Check for updates

Chemical looping hydrogen production with modified iron ore as oxygen carriers using biomass pyrolysis gas as fuel

Tingting Xu,[a] Bo Xiao,[a] Gensheng Fu,[a] Sicheng Yang[b] and Xun Wang [ID] *[a]

The chemical looping hydrogen (CLH) production was conducted in a fluidized bed reactor with the modified iron ore oxygen carriers (OCs) using simulated biomass pyrolysis gas (BPG) as fuel. Both carbon capture efficiency and hydrogen yield increased with the elevated reaction temperature in the fuel reactor (FR). As the reduction time in the FR increased, the carbon capture efficiency decreased but the hydrogen yield increased. An FR temperature of 900 °C and reduction time of 40 min in the FR were optimal conditions for CLH production. At this condition, the carbon capture efficiency for the NiO–iron ore, CuO–iron ore CeO–iron ore and iron ore were 83.29%, 82.75%, 70.05% and 40.46%, respectively. The corresponding hydrogen yield and hydrogen purity were 8.89 mmol g^{-1} and 99.02%, 7.78 mmol g^{-1} and 99.68%, 6.25 mmol g^{-1} and 99.52%, and 2.45 mmol g^{-1} and 97.46%, respectively. The presence of NiFe$_2$O$_4$, CuFe$_2$O$_4$ and CeFeO$_3$ in the modified iron ore samples enhanced the reactivity of the iron ore and promoted its reduction. Both NiO–iron ore and CeO$_2$–iron ore exhibited good cycle performance, while the sintering of the CuO–iron ore resulted in a decrease in the reactivity. Compared with the CuO–iron ore and CeO–iron ore, the NiO–iron ore was more appropriate for hydrogen production due to its high hydrogen yield and good cycle performance.

1 Introduction

Hydrogen, an excellent energy carrier with high energy density and environmentally friendly properties, is considered a promising alternative energy source toward resolving the depletion of fossil fuels and environmental issues, such as the pollutant and greenhouse gas emissions.[1] More than 80% hydrogen around the world is produced by the steam reforming technology using fossil fuel as feedstock.[2] However, this technology has disadvantages, such as high energy consumption, a low energy integration efficiency, and serious CO$_2$ emissions.[2] Chemical looping hydrogen (CLH) production has received a great deal of attention in recent years because it can produce high purity hydrogen, and also capture carbon dioxide.[3,4] Furthermore, the negative CO$_2$ emissions can be achieved in CLH production using the carbon neutral biomass derived fuels, such as bio-oil, syngas and biochar.[5]

It is very crucial to select a suitable oxygen carrier (OC) in the CLH production process. Metal oxides, such as the oxides of Ce, Fe, Cu, Ni, Co and Mn, have been proposed as possible OCs for the hydrogen production.[6-10] Among various metal oxides, Fe$_2$O$_3$ was considered an ideal candidate for CLH production

due to its favorable thermodynamics, low cost, nontoxicity and environmentally friendly properties in Nature.[11] However, Fe$_2$O$_3$ cannot be regenerated completely just using steam as the oxidizing medium due to the limitation of the thermodynamic property. An air reactor is needed to oxide the reduced oxygen carrier. Therefore, as shown in Fig. 1, a three-reactor CLH production system was developed.[4,12] The three-reactor CLH production system consists of a fuel reactor (FR), a steam reactor (SR) and an air reactor (AR). Fe$_2$O$_3$ is reduced to Fe and FeO by fuel in the FR first, and then Fe and FeO are oxidized to Fe$_3$O$_4$ by steam to obtain hydrogen in the SR where the water splitting occurs. High purity hydrogen is produced. Afterwards, Fe$_3$O$_4$ is transferred back to the AR where it is oxidized to Fe$_2$O$_3$ by air.

In fact, a rapid decrease in the reactivity of pure iron oxide was observed during the redox cycles, due to agglomeration and sintering of Fe and Fe$_3$O$_4$ during the chemical looping processes. A large number of studies have been done to enhance the reactivity, stability and cycle performance of the Fe-based OCs by adding some metal oxides. Ordinarily, these OCs involve the formation of new compounds, which may have a higher reactivity and enhanced reduction rate.[13] Huang *et al.*[14] illustrated that iron ore modified by NiO was appropriate in the CLR with biomass char owing to the fact that the formation of the spinel-type nickel iron oxide NiFe$_2$O$_4$ improved the reaction rate of char gasification. Chen *et al.*[15] reported that the NiO addition improved the maximum reaction rate of the iron-based

[a] School of Environmental Science & Engineering, Huazhong University of Science & Technology, Wuhan 430074, China. E-mail: xunw@hust.edu.cn; Tel: +86 15271949823

[b] China Urban Construction Design & Research Institute Co., Ltd. (CUCD), China
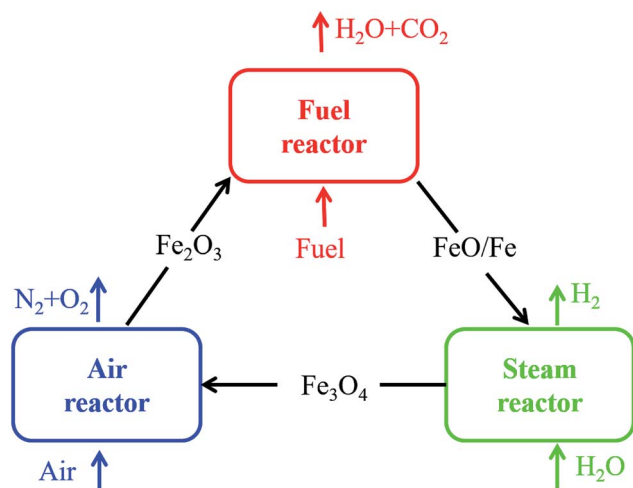
Fig. 1 Schematic of the three-reactor CLH production system.

OCs in the oxidation stage and promoted the further reduction of Fe-oxides to Fe. Ismail et al.[16] demonstrated that the CaO-modified Fe_2O_3 OCs exhibited higher reactivity and higher stability compared to the unmodified Fe_2O_3. Siriwardane et al.[17] found that the presence of Cu promoted the deeper reduction of Fe_2O_3, and improved the oxidation and reduction rates. Sun et al.[18] confirmed that CeO_2 could effectively inhibit carbon deposition or Fe_3C formation in CLH production with iron-based oxygen carriers.

Natural iron ore, as one of the iron-based OCs, have been intensively studied in chemical looping processes due to their lower application cost.[19–22] In recent years, natural iron ores have been gradually applied to the CLH production process. Zeng et al.[23] investigated the bio-oil CLH production process using an Austrian MAC iron ore as the OC. The hydrogen purity and hydrogen yield at 96% and 635 mL per mL oil, respectively, were achieved with a steam-to-oil ratio of 1.5. Xiao et al.[24] found that the carbon and Fe_3C formation led to a decrease in the reducibility of the four iron-based natural minerals. In general, the low redox reactivity is the main issue with using natural iron ore as OCs.[25–28]

Similarly, few studies have been reported in which the metals, Na, K, Cu and Ca etc., were implemented to enhance the reactivity of natural iron ores. Wang et al.[29] reported that adding K and Cu had significant effects on enhancing the reduction reactivity of hematite, as well as elevating the hydrogen production in the CLH production process. Liu et al.[30] reported that the presence of K decreased the carbon deposition, and increased the reduction rate of iron ore and hydrogen yield in CLH production. Gu et al.[31] confirmed the feasibility of CLH production using the mixture of iron ore and biomass ash as OCs. Although some encouraging results were presented in the abovementioned studies, the issues of modified iron ores (such as sintering, agglomeration and volatilization of modified components) still exist.[26,30,32,33] It is necessary to explore the modified iron ore OC with high reactivity and long-term stability for high purity hydrogen production.

In this study, the feasibility of CLH production with biomass pyrolysis gas using modified iron ore as OCs was evaluated. Modified iron ores (M_xO_y–iron ore, M = Ni, Cu and Ce) were prepared by the sample impregnation method. The CLH production experiments were conducted in a laboratory-scale fluidized bed reactor. The carbon capture efficiency, hydrogen yield, hydrogen purity and the reactivity of the OCs in CLH production process were investigated. The fresh and used OCs were characterized to evaluate their performance.

2 Experimental

2.1 Raw materials

The powder sample of the raw iron ore was obtained from the Wuhan Iron and Steel (Group) Company, which was supplied by the Chengchao iron ore miner, Ezhou, Hubei, China. The raw iron ore powder was first calcined at 900 °C for 6 h under atmospheric air. Then, the iron ore was grinded and sieved to 60–250 μm for use. The chemical components of the calcined iron ore were determined by X-ray fluorescence (XRF) spectroscopy. The results are given in Table 1.

In this study, a simulated biomass pyrolysis gas (BPG) was used to reduce the OCs in the fluidized-bed reactor. The BPG ($10\% \ H_2 + 10\% \ CO + 5\% \ CH_4 + 75\% \ N_2$ balance) was purchased from the XiangYun Industry Co., Ltd. (Wuhan, China). All chemicals used in this research study were of analytical grade, and purchased from the Sinopharm Chemical Reagent Co., Ltd. (Shanghai, China).

2.2 Preparation of OCs

The modified iron ore OCs, M_xO_y–iron ore (M_xO_y = NiO, CuO and CeO_2) were prepared via the incipient wetness impregnation method. The mass fraction of NiO, CuO and CeO_2 were fixed at 10 wt% for all OCs. First, $Ni(NO_3)_2 \cdot 6H_2O$, $Cu(NO_3)_2 \cdot 3H_2O$ and $Ce(NO_3)_4 \cdot 6H_2O$ were accurately weighed and dissolved in deionized water to obtain nitrate aqueous solutions. Then, the aqueous solutions of $Ni(NO_3)_2 \cdot 6H_2O$, $Cu(NO_3)_2 \cdot 3H_2O$ and $Ce(NO_3)_4 \cdot 6H_2O$ were each transferred to the beaker containing iron ore powder. The resulting mixtures were stirred slowly at 80 °C for 12 h, dried at 105 °C for 48 h in a drying oven, and calcined at 1000 °C for 6 h in a muffle furnace. Finally, the resulting sample was cooled to room temperature, crushed, and sieved into particles with a size range of 50 μm to 430 μm for use.

2.3 Chemical looping hydrogen tests

The CLH production experiments were carried out in a fluidized-bed reaction system under atmospheric pressure, as shown in Fig. 2. This system consisted of a carrier gas unit,

Table 1 The elemental content of the calcined iron ore

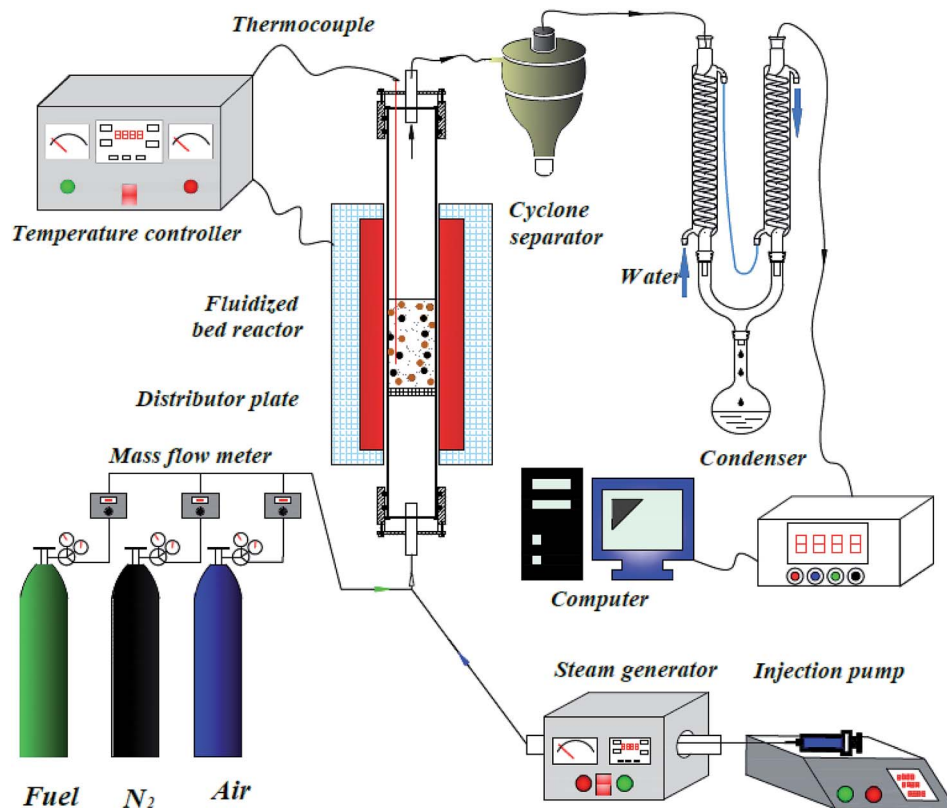| Oxide	Al	Si	Ca	Mg	Fe
wt%	2.68	3.19	2.17	2.81	88.15

Fig. 2   Reactor system for chemical looping hydrogen production.

fluidized bed reactor, cyclone separator, condenser, and on-line gas analyzer, steam generator and an injection pump.

A quartz tube (i.d. = 30 mm, length = 1000 mm) was used as the fluidized bed reactor, with a porous distributor plate placed in the reactor at a distance of 400 mm from the bottom. The temperature of the fluidized bed reactor was measured by a K-type thermocouple. The water was injected into the steam generator by an injection pump to obtain steam. The steam was introduced into the fluidized-bed reactor *via* a tube, which was wrapped by a heated bend. The temperatures of the steam generator and the heated bend were fixed at 300 °C and 180 °C, respectively.

The CLH production tests can be divided into three stages, namely the reduced stage, steam-oxidized stage and regenerated stage. Prior to each test, 20.0 g OCs were loaded onto the porous distributor plate in the fluidized-bed reactor. Next, the fluidized-bed reactor was heated to the desired temperature in air (500 mL min⁻¹). When the temperature was stable, air was then switched to nitrogen (500 mL min⁻¹) to sweep the fluidized-bed reactor for 10 min. In the reduced stage, BPG (500 mL min⁻¹) was introduced in the fluidized-bed reactor to reduce the OC particles. The reduction time was an important control variable, which changed from 20 min to 60 min with an interval of 10 min. Once the reaction ran out of time, BPG was switched to nitrogen (500 mL min⁻¹) to purge the reactor for 10 min. In the steam-oxidized stage, nitrogen (500 mL min⁻¹) was used as a carrier gas, and the steam was introduced to the

reactor to obtain high purity hydrogen for 60 min. The steam flow was 1.0 mL min⁻¹ in all tests, which was controlled by an injection pump. In the regenerated stage, air (500 mL min⁻¹) was used to regenerate the OCs for 60 min.

The flue gases passed through a cyclone separator, condenser, and on-line gas analyzer (Gasboard-3100, Wuhan Cubic Optoelectronics Co., Ltd.) in order. The gas concentrations (including CO, CO_2, CH_4, H_2 and O_2) were analyzed and recorded continuously, with the fine particles being collected and the condensable components of the flue gases being removed.

2.4   Data analysis

In the reduced stage, 500 mL min⁻¹ of BPG was used in the FR. The molar flow of N_2 ($F_{N_2\text{-FR}}$, mol s⁻¹) is a constant in the outlet.

The outlet gas molar flow ($F_{\text{out-FR}}$, mol s⁻¹) is calculated as

$$F_{\text{out-FR}} = \frac{F_{N_2\text{-FR}}}{1 - \sum x_i} \tag{1}$$

where x_i denotes the molar fraction of the gas components ($i =$ CO_2, CO, CH_4 and H_2).

The carbon capture efficiency (δ_c, %) is used to evaluate the conversion degree of carbonaceous gases into CO_2 in the fuel reactor. It was calculated as

$$\delta_C = \frac{\int_{t_0}^{t_1} F_{\text{out-FR}} x_{CO_2} \mathrm{d}t}{\int_{t_0}^{t_1} F_{\text{out-FR}}(x_{CO} + x_{CO_2} + x_{CH_4}) \mathrm{d}t} \times 100\% \tag{2}$$

where t_0 *and* t_1 denote the start and end reaction times in the FR, respectively.

Similarly, the outlet N_2 flow ($F_{N_2\text{-SR}}$, 500 mL min^{-1}) is used as a carrier gas in the steam-oxidized stage. The outlet gas flow ($F_{\text{out-SR}}$, mol s^{-1}) is calculated as

$$F_{\text{out-SR}} = \frac{F_{N_2\text{-SR}}}{1 - \sum y_i} \qquad (3)$$

where y_i denotes the molar fraction of the gas components in the SR (i = CO_2, CO, CH_4 and H_2).

The total volume of hydrogen V_H (L) in the gas products is calculated as:

$$V_H = 22.4 \int_{t_2}^{t_3} F_{\text{out-SR}} y_{H_2} dt \qquad (4)$$

where t_2 denotes the reaction time in the steam reactor.

The hydrogen yield, H_y (mmol g^{-1}), is calculated as

$$H_y = \frac{1000 V_H}{22.4 m_{OC}} \qquad (5)$$

where m_{OC} (g) is the mass of the OC in each test.

The hydrogen purity (H_p) is calculated as

$$H_p = \frac{y_{H_2}}{\sum_i y_i} \times 100\% \qquad (6)$$

2.5 Characterization technologies of the OCs

An X'Pert PRO diffractometer (X'Pert PRO, PANalytical B.V.) equipped with a Cu Kα radiation source (40 kV and 40 mA) was used to obtain X-ray diffraction (XRD) patterns of the OCs. The OCs were scanned at a rate of 2° min^{-1} from $2\theta = 10°$ to 80° with a scanning step of 0.02°. N_2 adsorption–desorption isotherms and pore-diameter distribution at −196 °C were measured using a Micrometrics ASAP 2010 system. The specific surface areas were calculated by the Brunauer–Emmett–Teller (BET) method. The surface morphology of the OCs was obtained using environmental scanning electron microscopy (ESEM; FEI Quanta 200) in conjunction with energy-dispersive X-ray spectroscopy (EDS). H_2-TPR was conducted in an AutoChem II 2920. First, the sample (about 0.20 g) was heated to 300 °C at a rate of 10 °C min^{-1} in helium (50 mL min^{-1}) and kept for 3 h. After being cooled to 50 °C, helium was replaced by a gas mixture consisting of 10/90H_2/Ar v/v% (50 mL min^{-1}), and the sample was reheated to 900 °C at a rate of 10 °C min^{-1}.

3 Results and discussion

In the FR, the OCs were reduced by BPG. The reduction time has a great effect on the carbon capture efficiency in the FR and the hydrogen yield in the SR. In this study, the reduction time in the FR increased from 20 min to 60 min. Both the hydrogen
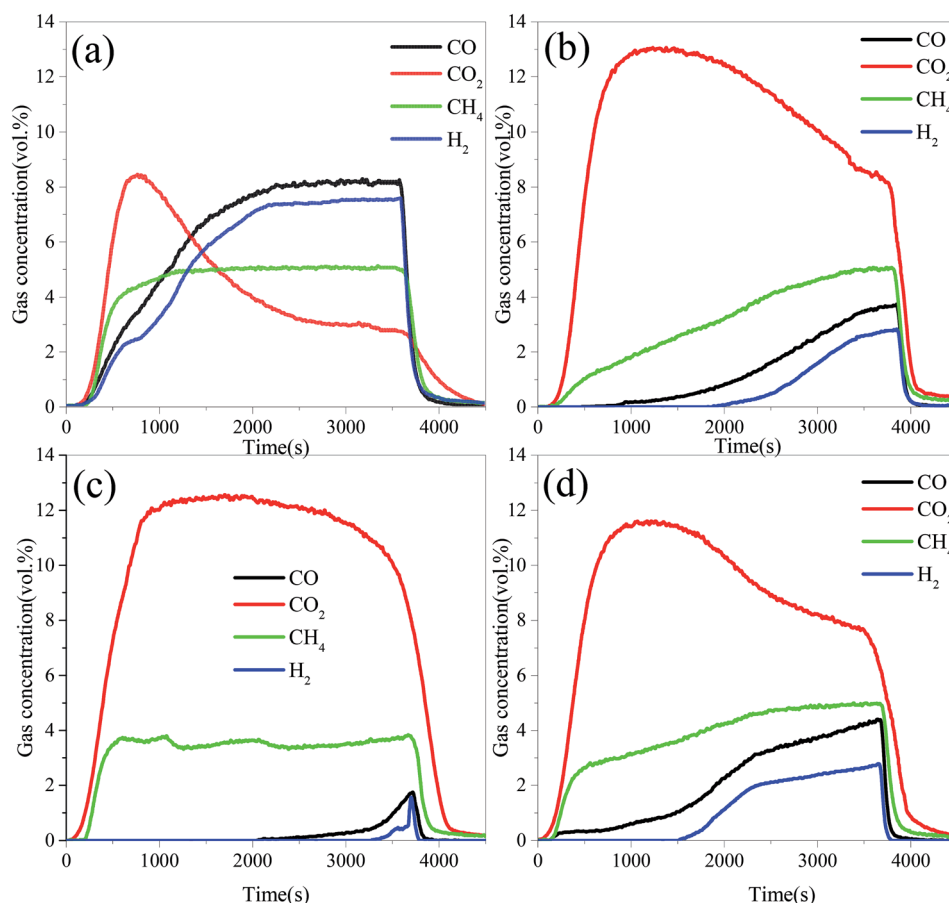
Fig. 3 Gas concentration profiles in the FR at 900 °C with different OCs.

production time in the SR and the regeneration time in the AR were fixed at 60 min. The reaction temperatures of the FR, SR, and AR were set at 900 °C.

3.1 Gas concentration profiles

Fig. 3 displays the variation trend of the gas concentration with reaction time in the FR at 900 °C. As can be seen, the main gas components were CO_2, CO, CH_4 and H_2 in the FR. At the beginning of the reaction, the reductive gases (CH_4, CO and H_2) were oxidized by lattice oxygen. Therefore, the CO_2 concentration for all OCs increased quickly. Subsequently, the unreacted reductive gases were measured, and their concentrations increased with the increase in the reduction time. It was implied that the lattice oxygen derived from OCs was consumed gradually with the increasing reaction time. At the same moment, the concentrations of CO_2 for all three modified OCs were higher than that for the iron ore, while the concentrations of CH_4, CO and H_2 showed the opposite tendency. These results indicated that the presence of the metal oxides significantly enhanced the reactivity of the iron ore. For the same modified OC, the concentration of CH_4 in the FR was the highest, followed by CO, and H_2 was the lowest. In fact, the concentrations of CO and H_2 in BPG were higher than that of CH_4. These results indicated that the selectivity of the modified iron ore OCs toward the three reductive gases (namely CO, H_2 and CH_4) follow the order of H_2 > CO > CH_4. This result was consistent with the reduction rate of Fe_2O_3 in the different reductive gases.[19,34,35] It was noted that the NiO–iron ore had the lowest concentration of CO and H_2, and the CuO–iron ore exhibited the lowest CH_4 concentration, indicating that the NiO–iron ore exhibited the highest selectivity toward CO and H_2. The CuO–iron ore had the highest selectivity toward CH_4.

The OCs were reduced by BPG for 60 min at 900 °C in the FR. After that, the steam was introduced into the reactor to produce hydrogen in the SR. Fig. 4 presents the gas concentration profiles in the SR. The H_2 concentration for the three OCs increased quickly, and then decreased. The instantaneous maximum H_2 concentration for the three modified iron ores was higher than 60%, while the peak value of the H_2 concentration for iron ore was just 38.75% under the same conditions. It was noted that a small amount of CO and CO_2 products was detected in the SR. It was attributed to the oxidation of carbon deposited onto the OCs during the reduction stage in the FR. Both CO and CH_4 can form carbon deposits through reactions (R1) and (R2) at relatively high temperatures. The carbon deposits formed on the surface of the OCs in the FR, and then reacted with steam in the SR to produce carbonaceous gases (R3 and R4), resulting in a decrease in the hydrogen purity.
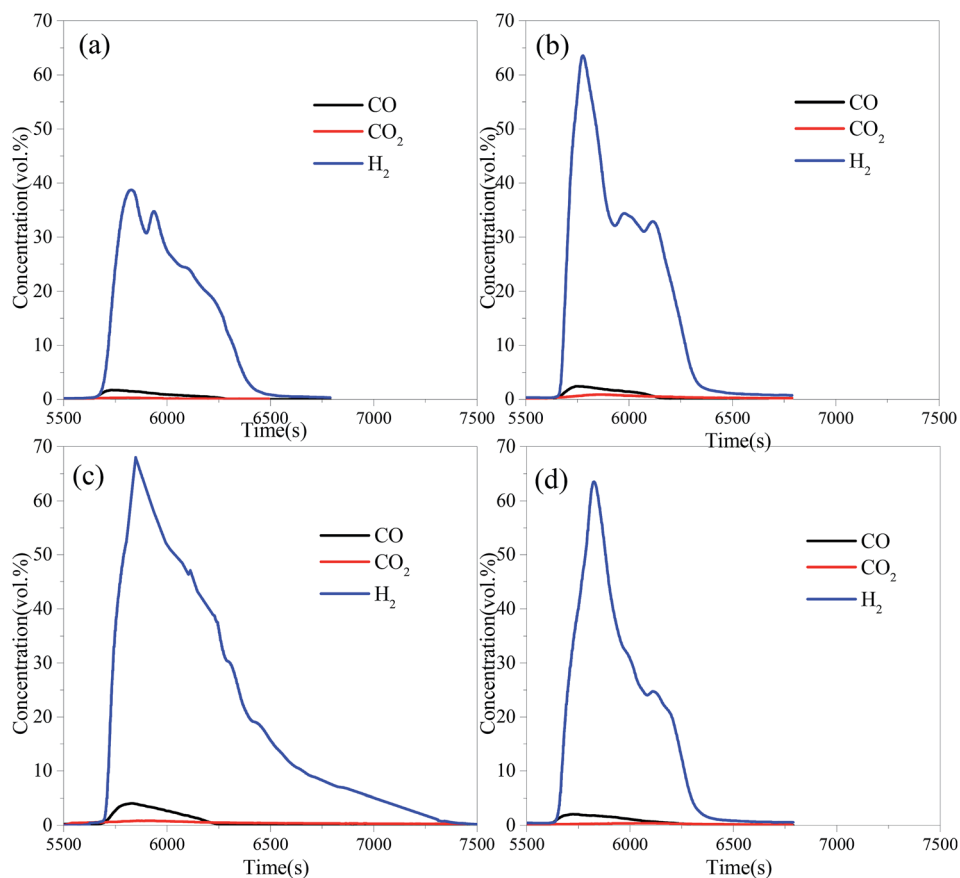

Fig. 4 The gas concentration profiles in the SR with different OCs reduced by BPG for 60 min at 900 °C: (a) iron ore, (b) CuO−iron ore, (c) NiO−iron ore and (d) CeO$_2$−iron ore.

$$2CO \Leftrightarrow CO_2 + C \tag{R1}$$

$$CH_4 \Leftrightarrow 2H_2 + C \tag{R2}$$

$$C + H_2O \Leftrightarrow H_2 + CO \tag{R3}$$

$$C + 2H_2O \Leftrightarrow 2H_2 + CO_2 \tag{R4}$$

3.2 Effects of the reduction time in FR

3.2.1 Carbon capture efficiency.
Fig. 5 shows the carbon capture efficiency in the FR for four OCs at 900 °C under different reduction times. In the initial stage, the carbon capture efficiency for the four OCs was close to 100%. The carbon capture efficiency decreased with the increase of the reduction time. The carbon capture efficiency for the CuO–iron ore, NiO–iron ore, CeO$_2$–iron ore and iron ore at 97.39%, 91.02%, 91.01% and 86.59%, respectively, were observed at a reaction time of 10 min. These values were then decreased to 75.90%, 80.30%, 65.61% and 33.75% at the reduction time of 60 min. At the beginning of the reaction, Fe$_2$O$_3$ was reduced readily into Fe$_3$O$_4$ by reductive gases, which favored the production of CO$_2$ and H$_2$O. With the increase in the reaction time, the conversion from Fe$_3$O$_4$ to FeO or Fe became difficult, and the reductive gases also were not converted completely into CO$_2$ and H$_2$O. Miguel et al.[36] have reported that iron ore can fully convert the simulated syngas at 880 °C, regardless of the CO/H$_2$ ratio used. However, lower conversion rates were observed with methane-containing fuels. Thus, it was inferred that the CH$_4$ in BPG was the main factor for the reduction of CGE. The CuO–iron ore exhibited the highest carbon capture efficiency until a reduction time around at 50 min. Compared with the NiO–iron ore and CeO$_2$–iron ore, the CuO–iron ore was more suitable for the application of the chemical looping combustion process for carbon capture. It was noted that there

was a slight decrease in the carbon capture efficiency for the NiO–iron ore OCs from 20 min to 60 min. The carbon capture efficiency for the CeO$_2$–iron ore was the lowest among the three modified iron ores at the same time. However, it was still much higher than that for iron ore. Compared with CuO and NiO, the oxygen transport capacity of CeO$_2$ can be negligible. Although the CeO$_2$–iron ore had a lower mass fraction of Fe$_2$O$_3$ than that of iron ore, the presence of CeO$_2$ promoted the reactivity of Fe$_2$O$_3$.

3.2.2 Hydrogen yield.
Fig. 6 shows the hydrogen yields for the four OCs under different reaction times. As the reaction time increased, the hydrogen yields for all OCs increased. This is mainly due to the fact that the reduction degree of the OCs was deepened with increasing reduction time in the FR. The maximum theoretical hydrogen yield of the iron ore was 14.36 mmol g^{-1}; in this condition, Fe$_2$O$_3$ in the iron ore was reduced completely into Fe. The theoretical hydrogen yield decreased to 3.59 mmol g^{-1} when the Fe$_2$O$_3$ in iron ore was reduced completely into FeO. When the reduction time was 20 min, a maximum hydrogen yield of 1.54 mmol g^{-1} was obtained for the iron ore. Thus, the Fe$_2$O$_3$ was reduced to FeO and Fe$_3$O$_4$ after 20 min. The hydrogen yields of the NiO–iron ore, CuO–iron ore, CeO$_2$–iron ore were 4.65 mmol g^{-1}, 5.36 mmol g^{-1} and 3.96 mmol g^{-1} after 20 min, respectively, indicating that Fe$_2$O$_3$ was reduced to FeO and Fe. Compared with the modified iron ore OCs, the iron ore exhibited a lower hydrogen yield under the same conditions, indicating that the presence of metal oxides improved the reactivity and enhanced the reduction degree of the iron ore. The hydrogen yields for the four OCs all decreased in the following order: NiO–iron ore > CuO–iron ore > CeO$_2$–iron ore > iron ore. The maximum hydrogen yields of the NiO–iron ore, CuO–iron ore, CeO$_2$–iron ore and iron ore were 11.46 mmol g^{-1}, 10.84 mmol g^{-1}, 10.44 mmol g^{-1} and 5.39 mmol g^{-1} at the reaction time of 60 min, respectively.

In general, more hydrogen can be obtained by increasing the reduction time in the FR. However, the longer the reduction
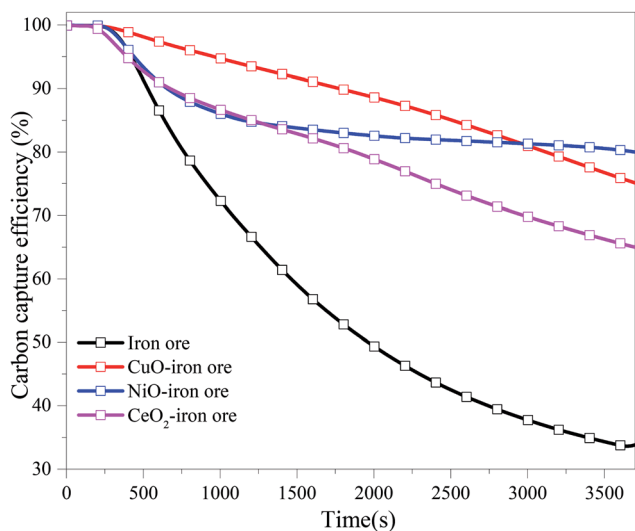

Fig. 5 The variation trend of the carbon capture efficiency (CGE) with reduction time in FR at 900 °C.
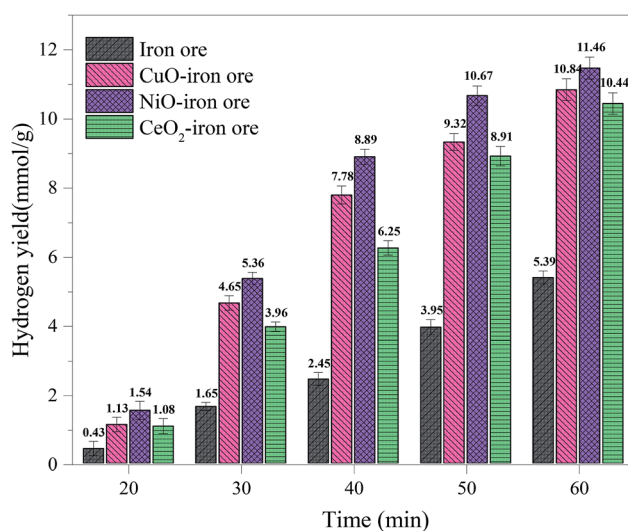

Fig. 6 The hydrogen yield in SR at 900 °C with different reduction times in FR.

time, the lower was the carbon capture efficiency. According to the comprehensive analysis of the hydrogen yield and carbon capture efficiency, it was concluded that the reduction time at ~40 min in the FR at 900 °C was an optimal value. Under this condition, the hydrogen yields of the four OCs in the SR were 8.89 mmol g^{-1}, 7.78 mmol g^{-1}, 6.25 mmol g^{-1} and 2.45 mmol g^{-1} for the NiO–iron ore, CuO–iron ore, CeO$_2$–iron ore and iron ore, respectively. In addition, the corresponding carbon capture efficiencies in the FR were 83.29%, 82.54%, 70.97% and 40.46%.

3.3 Effects of the reaction temperatures in FR

Temperature plays a key role in all chemical looping processes. In the CLH production process, temperature directly affected the carbon capture efficiency in the FR, hydrogen yield and purity in the SR and the regeneration rate of the OCs in the AR. In this section, the temperature effects were investigated. In each run, the reaction temperatures of the FR, SR and AR were identical. The reaction temperatures varied in the range of 800–1000 °C with an interval of 50 °C. The reduction time of the OCs in the FR by BPG was 40 min, the oxidation time of the OCs in the SR by steam was 60 min and the regeneration time of the OCs in the AR by air was 60 min.

3.3.1 Carbon capture efficiency. As shown in Fig. 7, with the increase of temperature from 800 °C to 1000 °C, the carbon capture efficiencies for the iron ore, CuO–iron ore, NiO–iron ore and CeO$_2$–iron ore increased from 32.11%, 76.65%, 70.66% and 62.86% to 48.69%, 88.33%, 89.19% and 80.65%, respectively. Compared with the CuO–iron ore and NiO–iron ore, the CeO$_2$–iron ore exhibited lower carbon capture efficiency in the whole temperature range. It was mainly attributed to the fact that the CuO–iron ore and NiO–iron ore provided more lattice oxygen for syngas combustion in comparison to the CeO$_2$–iron ore. The carbon capture efficiency for the CuO–iron ore was higher than that for NiO–iron ore at 800 °C and 850 °C, while an opposite tendency was observed when the reaction temperature reached above 900 °C. This indicated that the activity of the CuO–iron

ore at a lower temperature was higher than that of the NiO–iron ore. It might be attributable to the fact that CuFe$_2$O$_4$ was more readily reduced than NiFe$_2$O$_4$ at a low temperature.[37,38]

3.3.2 Hydrogen yield and purity. Fig. 8 shows the hydrogen yield at different reaction temperatures with the reduction time of 40 min in the FR. The hydrogen yield, 1.54 mmol g^{-1}, 1.03 mmol g^{-1} and 0.88 mmol g^{-1}, for the NiO–iron ore, CuO–iron ore and CeO$_2$–iron ore, respectively, were obtained at 800 °C. The temperature not only affected the reaction reactivity of the OCs with fuel, but also affected the reaction reactivity of the OCs with steam. With the reaction temperature increased to 900 °C, the hydrogen yields at 8.89 mmol g^{-1}, 7.78 mmol g^{-1} and 6.25 mmol g^{-1} for the NiO–iron ore, CuO–iron ore and CeO$_2$–iron ore were observed, respectively. When the temperature was higher than 900 °C, the effect of increasing the temperature on the hydrogen yield was not obvious. It was attributed that the reduction from FeO to Fe was difficult even at a high temperature. The highest hydrogen yields of 11.23 mmol g^{-1}, 11.03 mmol g^{-1} and 9.89 mmol g^{-1}, for the NiO–iron ore, CuO–iron ore and CeO$_2$–iron ore were obtained at 1000 °C for 60 min, respectively.

Generally, a high concentration of hydrogen can be obtained in the steam-iron process. In fact, small amounts of carbonaceous gas were observed in the SR, which were derived from the reactions between the deposited carbon and H$_2$O. The carbon deposition not only decreased the reactivity of the OCs, but also contaminated the hydrogen produced in the steam oxidation stage, leading to the reduction in the hydrogen purity. Fig. 9 shows the varying trend of the hydrogen purity at different reaction temperatures. With the increase of temperatures of the FR, the hydrogen purity decreased. It was attributed to the fact that the high temperature enhanced the reactivity of OCs and promoted the subsequent BPG oxidation process. Therefore, the carbon deposition on the surface of the OC increased. At the same temperature, the hydrogen purity of the iron ore was
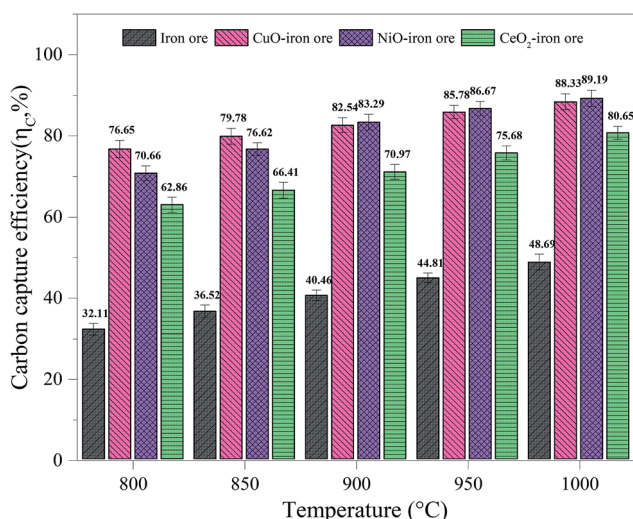

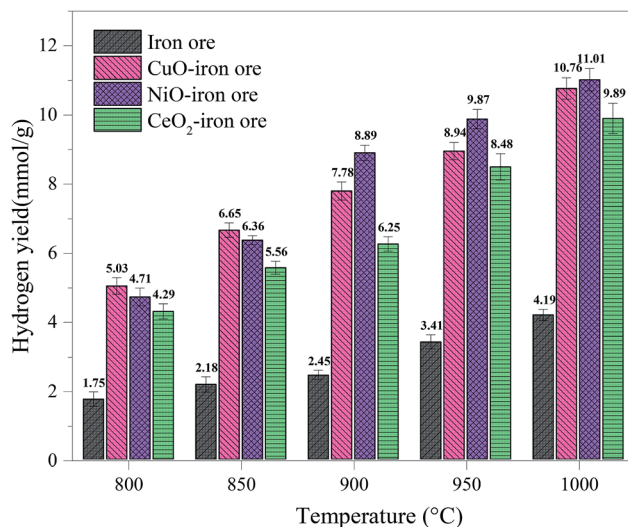Fig. 7 The carbon capture efficiency in FR at different temperatures.

Fig. 8 Effect of the reduction temperature in FR on the hydrogen yield in SR.
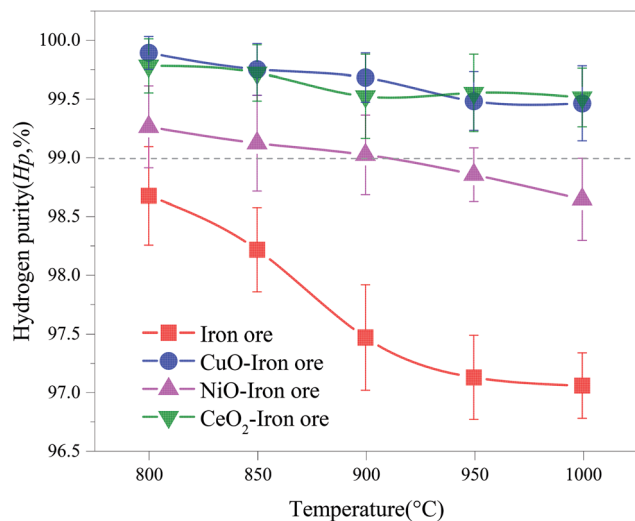
Fig. 9 Effect of the reduction temperature in FR on the hydrogen purity in SR.

Fig. 10 The various trends of the carbon capture efficiency and hydrogen yield in the cyclic test.

lowest. This result confirmed that the addition of CuO, NiO and CeO$_2$ played a role in inhibiting the carbon deposition. A hydrogen purity of >99.0% was achieved in the temperature range of 800–1000 °C using both CuO–iron ore and CeO$_2$–iron ore as the OC. The hydrogen purity for the NiO–iron ore decreased from 99.26% at 800 °C to 98.64% at 1000 °C. Zeng et al.[39] reported that the hydrogen yield and hydrogen purity varied from 1.66 mmol and 99% from to 2.81 mmol and 84%, respectively, when using a bio-oil heavy fraction as fuel and Fe$_2$O$_3$/Al$_2$O$_3$ (60 wt%/40 wt%) as the OC at 950 °C. Both the CuO–iron ore and CeO$_2$–iron ore showed higher anti-coking ability compared with the NiO–iron ore. It was attributed to the fact that the metallic Fe and Ni in the deeply reduced OC have good catalytic performances for the CH$_4$ decomposition reaction (R2).

3.4 Cyclic tests

In order to investigate the cyclic performance of the modified iron ore OCs, a total of 10 cycles were conducted in the fluidized bed reactor. The temperatures of the FR, SR and AR were 900 °C. The reduction time in the FR, steam oxidation time in the SR and regeneration time in the AR were 40 min, 60 min and 60 min, respectively. As shown in Fig. 10, the carbon capture efficiency and hydrogen yield for the CuO–iron ore OC decreased from 82.54% and 7.78 mmol g^{-1} to 75.09% and 6.38 mmol g^{-1} with increasing cycles, respectively. The carbon capture efficiency increased slightly to 78.14% in a cyclic test of the CeO$_2$–iron ore, and there was no significant trend change for the hydrogen yield. After 10 cycles, a hydrogen yield of 6.33 mmol g^{-1} was observed for the CeO$_2$–iron ore. The carbon capture efficiency and hydrogen yield for the NiO–iron ore both decreased slightly, and achieved 79.51% and 8.89 mmol g^{-1} at the 10th cycle, respectively. These results indicated that the CeO$_2$–iron ore and NiO–iron ore had good cyclic performances, while the reactivity of the CuO–iron ore decreased with an increase in the number cycle.
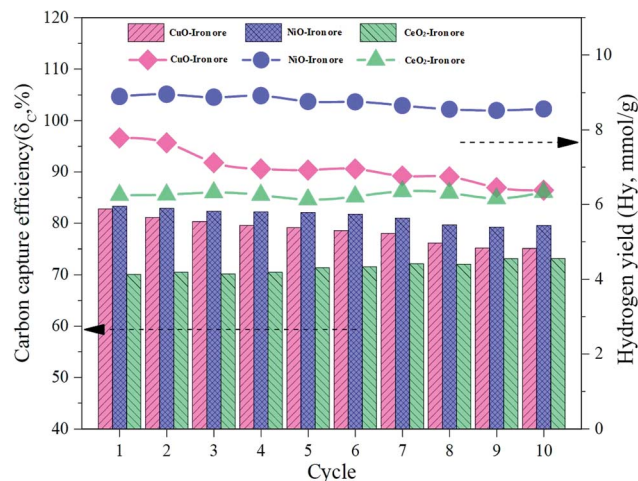
3.5 Characterization of the OCs

3.5.1 H$_2$-TPR.
The H$_2$-TPR profiles of different fresh OCs were processed using the peak-fitting software. The results are shown in Fig. 11. The different colored curves present the reduction of different species. Three peaks at ca. 495 °C, 630 °C and 770 °C were observed for the H$_2$-TPR profiles of the fresh
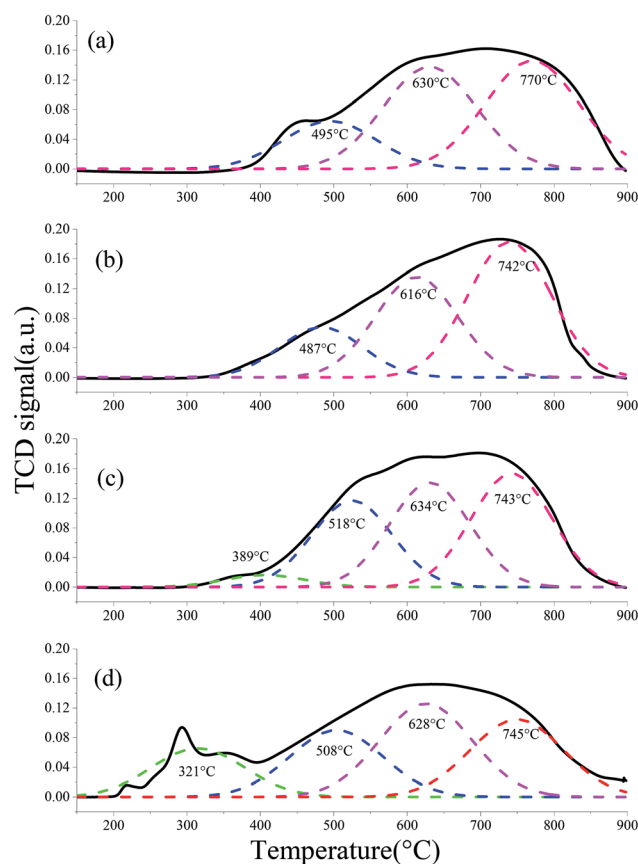

Fig. 11 H$_2$-TPR profiles of the fresh OCs: (a) iron ore, (b) CeO$_2$–iron ore, (c) NiO–iron ore and (d) CuO–iron ore.

iron ore, which were assigned to the reduction of Fe_2O_3, Fe_3O_4 and FeO, respectively. Similar results were published by Gu et al.[40] Similarly, the fresh CeO_2–iron ore exhibited three reduction peaks. The first peak at ca. 470 °C was attributed to the reduction of residual surface Fe^{3+}. However, the reduction peaks for the CeO_2–iron ore shifted to lower temperatures compared with the peaks for the iron ore, indicating that the CeO_2 additive decreased the reduction temperature of the iron ore. When the iron ore was modified by NiO and CuO, reduction peaks at 389 °C and 321 °C appeared and were assigned to the reduction of free NiO and CuO located on the surface, respectively. Compared with the iron ore, two peaks with larger peak areas were observed at 518 °C for the NiO–iron ore and at 508 °C for the CuO–iron ore, assigned to the reduction of $NiFe_2O_4$ and $CuFe_2O_4$. Similar results were observed in our previous work.[37] The peaks at about 630 °C were similar for the NiO–iron ore, CuO–iron ore and iron ore, indicating that the additives had a small influence on the reduction of Fe_3O_4. Similar to that of the CeO_2–iron ore, the peaks at 743 °C for the NiO–iron ore and at 745 °C for the CuO–iron ore verified that the reduction temperature of the iron ore was decreased by introducing metallic oxides.

3.5.2 XRD. The crystal phases of the OCs at different reaction stages are listed in Table 2. The main components of the calcined iron ore were Fe_2O_3 and SiO_2. For the fresh modified iron ore OCs, Fe_2O_3 and the metal oxides (namely CuO, NiO and CeO_2) were correspondingly presented. Generally, CuO and NiO had higher oxygen transport capacities than Fe_2O_3 in the chemical looping process, and more lattice oxygen derived from CuO and NiO was beneficial to enhancing the syngas conversion. Additionally, $CuFe_2O_4$ and $NiFe_2O_4$ with spinel structures (AB_2O_4) were observed in the CuO–iron ore and NiO–iron ore samples, respectively. Intensive references demonstrated that the presence of a spinel structure improved the reduction kinetics and enhanced the reducibility of Fe_2O_3.[14,41–44]

In the reduced samples, the unmodified iron ore was mainly reduced into FeO and Fe_3O_4; the CuO–iron ore was reduced into Cu, FeO and Fe; the NiO–iron ore was reduced into Ni, FeO, (Ni, Fe) and Fe; while the CeO_2–iron ore was reduced into FeO, $CeFeO_3$ and Fe. The reduction of Fe_2O_3 to Fe_3O_4 did not contribute to the production of hydrogen in the oxidation step. Therefore, the unmodified iron ore displayed the lowest hydrogen yield. The Fe_3O_4 phase was not observed in the modified OCs after the reduction reaction. These results suggested that the metal oxides promote the reduction of Fe_3O_4. It was noted that $CeFeO_3$ with a perovskite structure (ABO_3) was detected in the reduced sample of the CeO_2–iron ore OC. Many
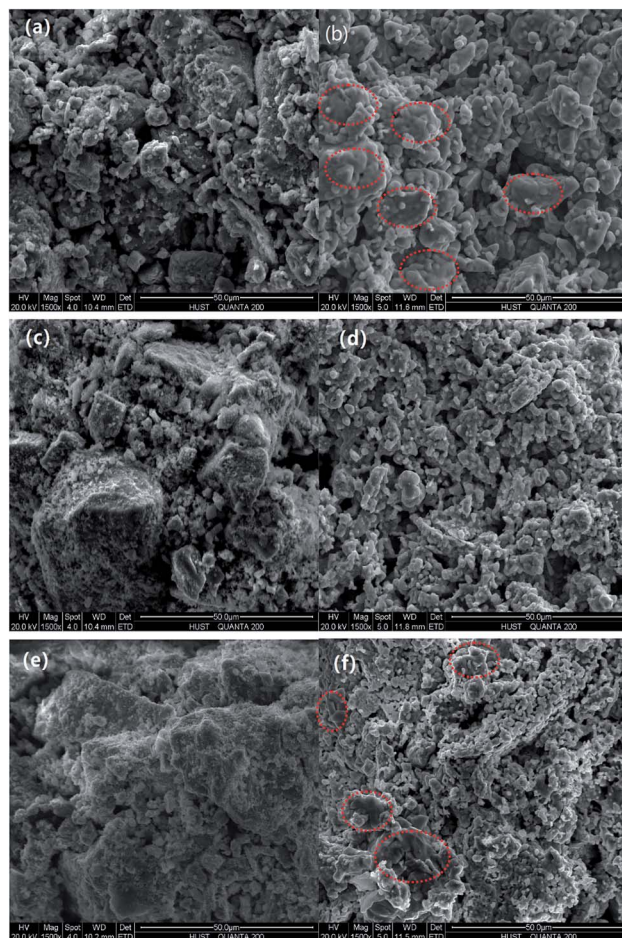

Fig. 12 The surface morphology of the three modified OCs particles: (a), (c) and (e) are the fresh CuO–iron ore, NiO–iron ore and CeO_2–iron ore, respectively; (b), (d) and (f) are the CuO–iron ore, NiO–iron ore and CeO_2–iron ore after 10 cycles, respectively.

researchers also reported that Fe_2O_3, together with CeO_2, forms a perovskite-type $CeFeO_3$, which improved the reversibility of the Fe_2O_3 redox reaction.[40,45–47] Gu et al.[40] reported that the abundant Ce^{3+} ions in $CeFeO_3$ might act as a catalyst to enhance the reducibility of the Ce and Fe oxides. Zhu et al.[47] found that the formation of $CeFeO_3$ enhanced the oxygen mobility of the CeO_2–Fe_2O_3 OC.

After the steam oxidation process, the Fe species contained in the OCs were mainly oxidized into Fe_3O_4 to produce hydrogen. When the CeO_2–iron ore was used as an OC, $CeFeO_3$ remained after the steam oxidation process. Thus, the Fe

Table 2 The component of crystalline phase of OCs in different reaction stages

Samples	Fresh	Reduced	Oxidized by H_2O	Oxidized by air	After 10 redox cycles
Iron ore	Fe_2O_3	FeO, Fe_3O_4	Fe_3O_4	Fe_2O_3	Fe_2O_3
CuO–iron ore	Fe_2O_3, CuO, $CuFe_2O_4$	FeO, Fe, Cu	Cu, Fe_3O_4	Fe_2O_3, $CuFe_2O_4$	Fe_2O_3, $CuFe_2O_4$
NiO–iron ore	Fe_2O_3, NiO, $NiFe_2O_4$	Ni,FeO, (Ni, Fe), Fe	Ni, Fe_3O_4	Fe_2O_3, $NiFe_2O_4$	Fe_2O_3, $NiFe_2O_4$
CeO–iron ore	Fe_2O_3, CeO_2	FeO, $CeFeO_3$, Fe	Fe_3O_4, $CeFeO_3$	Fe_2O_3, CeO_2	Fe_2O_3, CeO_2

element contained in $CeFeO_3$ was not oxidized by steam to produce hydrogen. This can be used to explain how the CeO_2–iron ore OC had a lower hydrogen yield in comparison with that of the CuO–iron ore and NiO–iron ore OCs.

In the regenerated samples, Fe_3O_4 was further oxidized to Fe_2O_3 by air in the AR. Both NiO and CuO disappeared and instead, $CuFe_2O_4$ and $NiFe_2O_4$ with a spinel structure were observed in the CuO–iron ore and NiO–iron ore OCs, respectively. It was due to the reaction of NiO and CuO with the iron ore during the redox cycles. $CeFeO_3$ was oxidized to CeO_2 and Fe_2O_3 by air. It was reported that $CeFeO_3$ was unstable in an oxidation atmosphere.[40] Compared with the components of the OCs at the first and tenth cycle, it can be found that the crystal phase of the OCs did not change significantly.

3.5.3 ESEM. Fig. 12 shows the SEM micrographs of the three modified OCs after 10 cycles, and the magnification was 1500 times. The different size particles adhered to the surface of the fresh CuO–iron ore. After 10 cycles, the particles became smooth and stuck together, resulting in the compact areas. This may be due to the presence of the sintering behavior of copper during the cyclic tests. Floccules were observed on the fresh

NiO–iron ore sample surface due to the NiO deposition during the preparation process. The floccules were reduced or even disappeared after 10 cycles and instead, formed more particles on the surface. Similar to the NiO–iron ore sample, the surface of the fresh CeO_2–iron ore was almost covered by the flocculent substance. After the cyclic experiments, it presented smaller regular particles. Compared with the NiO–iron ore sample, a slight agglomeration was observed for the CeO_2–iron ore after 10 cycles.

3.5.4 EDS. Fig. 13 exhibits the distribution of elements on the surface of the reduced OCs. Cu, Ni and Ce were observed on the surfaces of the reduced CuO–iron ore, NiO–iron ore and CeO_2–iron ore OCs, respectively. Additionally, some trace elements (C, Ca and Si) were also examined. This result indicated the formation of carbon deposition during the reduction reaction. The largest carbon atom content at 12.13 wt% was observed on the surface of the reduced iron ore. The carbon atom content for the reduced CuO–iron ore, NiO–iron ore and CeO_2–iron ore were 7.58 wt%, 8.25 wt% and 7.72 wt%, respectively. The introduction of the metal oxides was beneficial to decreasing the carbon deposition. The carbon deposition
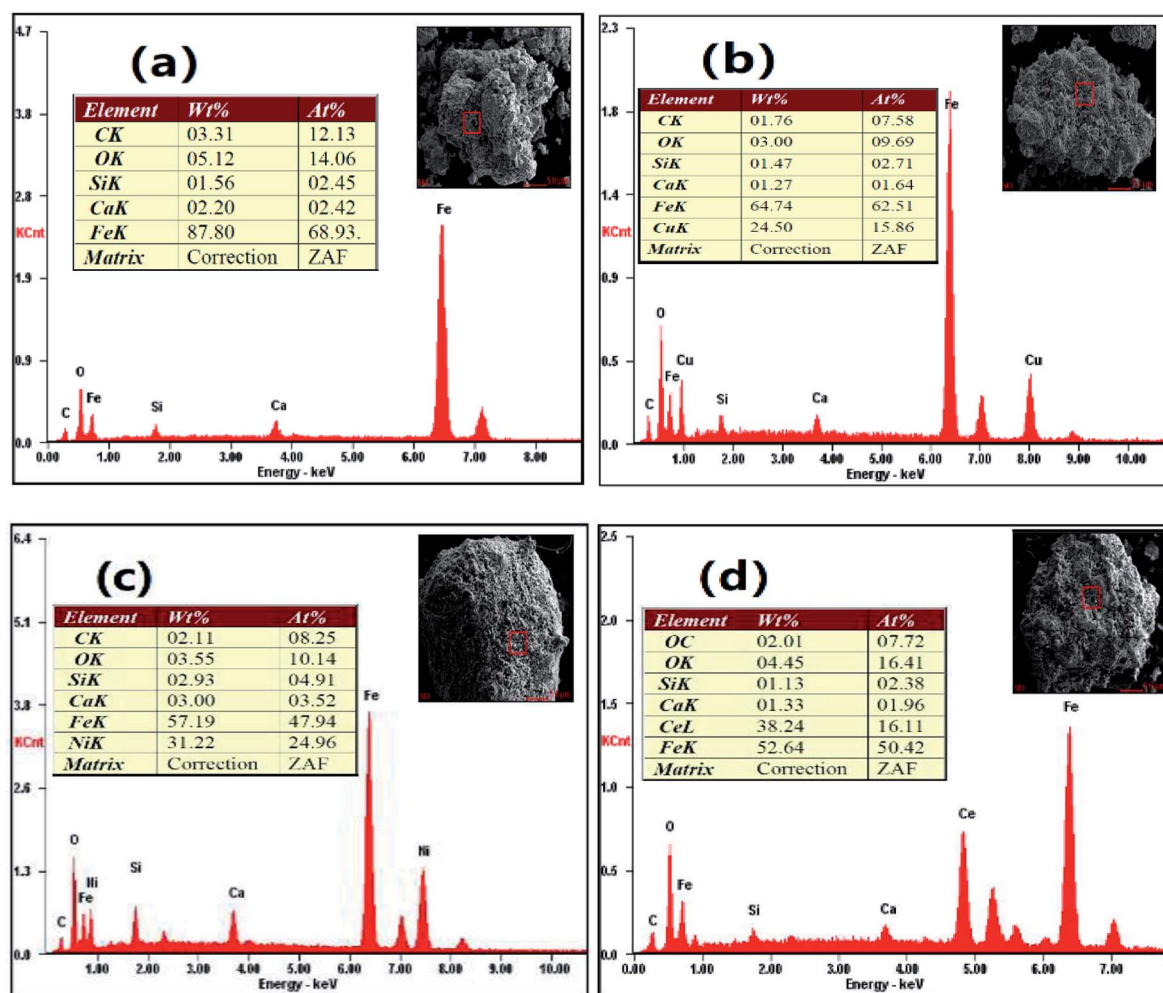

(a)

Element	Wt%	At%
CK	03.31	12.13
OK	05.12	14.06
SiK	01.56	02.45
CaK	02.20	02.42
FeK	87.80	68.93.
Matrix	Correction	ZAF

(b)

Element	Wt%	At%
CK	01.76	07.58
OK	03.00	09.69
SiK	01.47	02.71
CaK	01.27	01.64
FeK	64.74	62.51
CuK	24.50	15.86
Matrix	Correction	ZAF

(c)

Element	Wt%	At%
CK	02.11	08.25
OK	03.55	10.14
SiK	02.93	04.91
CaK	03.00	03.52
FeK	57.19	47.94
NiK	31.22	24.96
Matrix	Correction	ZAF

(d)

Element	Wt%	At%
OC	02.01	07.72
OK	04.45	16.41
SiK	01.13	02.38
CaK	01.33	01.96
CeL	38.24	16.11
FeK	52.64	50.42
Matrix	Correction	ZAF

Fig. 13 The distribution of elements on the surface of the OCs after reduction reaction in FR at 900 °C. (a) Iron ore, (b) CuO−iron ore, (c)NiO−iron ore and (d) CeO_2−iron ore.

Table 3 The specific areas, total pore volumes, and average pore diameters of the fresh and after 10 cycles OCs

Samples	Fresh OCs			OCs after 10 cycles		
	Specific areas ($m^2\ g^{-1}$)	Average pore diameter (nm)	Total pore volumes ($cm^3\ g^{-1}$)	Specific areas ($m^2\ g^{-1}$)	Average pore diameter (nm)	Total pore volumes ($cm^3\ g^{-1}$)
Iron ore	0.303	7.87	0.0015	0.201	7.33	0.0019
CuO–iron ore	0.746	8.46	0.0017	0.422	10.76	0.0022
NiO–iron ore	0.603	10.91	0.0022	0.582	11.62	0.0016
CeO$_2$–iron ore	0.549	7.24	0.0019	0.513	8.64	0.0017

resistance of the four oxygen carriers decreased in the following order: CuO–iron ore > CeO$_2$–iron ore > NiO–iron ore > iron ore, which is consistent with the change trend observed for hydrogen purity.

3.5.5 BET. Table 3 summarizes the specific areas, total pore volumes, and average pore diameters of the fresh and 10 cycle OCs. The fresh iron ore exhibited a small specific area (0.303 $m^2\ g^{-1}$) and total pore volume (0.0015 $cm^3\ g^{-1}$), indicating that it was not a porous material, which was not favorable to the gas diffusion in the chemical looping process. The specific areas of the OCs increased after loading with metal oxides. This was attributed to the metal oxides deposited on the surface of the iron ore. The fresh CuO–iron ore exhibited the highest specific area, 0.746 $m^2\ g^{-1}$, among the three modified OCs, but it decreased significantly to 0.422 $m^2\ g^{-1}$ after 10 cycles. The specific area decreased slightly from 0.603 $m^2\ g^{-1}$ and 0.549 $m^2\ g^{-1}$ to 0.582 $m^2\ g^{-1}$ and 0.513 $m^2\ g^{-1}$ for the NiO–iron ore and CeO$_2$–iron ore during the cycle tests, respectively. Combined with the results of the cycle tests, we can conclude that the NiO–iron ore and CeO$_2$–iron ore both had higher sintering resistance and thermal stability than the CuO–iron ore.

4 Conclusions

The CLH production process with the modified iron ore as OCs was conducted in a fluidized-bed reactor, where the OCs were first reduced by simulated BPG and then reacted with steam to produce H$_2$, and finally fully oxidized by air. The carbon capture efficiency increased with the decrease in the reduction time, but it presented an opposite trend as the temperature increased in the FR. Increasing the reduction temperature and time can improve the hydrogen yield. It was concluded that a condition of 900 °C with the reduction time of 40 min was suitable for hydrogen production and carbon capture. At this condition, the carbon capture efficiency for the NiO–iron ore, CuO–iron ore and CeO–iron ore were 83.29%, 82.75% and 70.05%, respectively. The corresponding hydrogen yield and purity were 8.89 mmol g^{-1} and 99.02%, 7.78 mmol g^{-1} and 99.68%, and 6.25 mmol g^{-1} and 99.52%, respectively. NiFe$_2$O$_4$, CuFe$_2$O$_4$ and CeFeO$_3$, which were observed in the CuO–iron ore and NiO–iron ore samples, enhanced the reactivity of the iron ore and promoted its reduction. Both NiO–iron ore and CeO$_2$–iron ore exhibited good cycle performances, while the sintering of the CuO–iron ore led to a decrease in the reactivity. Although the NiO–iron ore exhibited the highest carbon deposition and the lowest hydrogen purity compared with the CuO–iron ore and CeO–iron ore, the NiO–iron ore was the best OC for hydrogen production due to its high hydrogen yield and high cycle performance.

Conflicts of interest

There are no conflicts to declare.

Acknowledgements

References

1 I. Dincer and C. Acar, *Int. J. Hydrogen Energy*, 2017, **42**, 14843–14864.
2 R. Kothari, D. Buddhi and R. L. Sawhney, *Renewable Sustainable Energy Rev.*, 2008, **12**, 553–563.
3 M. Luo, Y. Yi, S. Wang, Z. Wang, M. Du, J. Pan and Q. Wang, *Renewable Sustainable Energy Rev.*, 2018, **81**, 3186–3214.
4 S. Ma, S. Chen, A. Soomro and W. Xiang, *Int. J. Hydrogen Energy*, 2017, **42**, 11006–11016.
5 T. Mendiara, F. García-Labiano, A. Abad, P. Gayán, L. F. de Diego, M. T. Izquierdo and J. Adánez, *Appl. Energy*, 2018, **232**, 657–684.
6 D. Zeng, S. Peng, C. Chen, J. Zeng, S. Zhang, H. Zhang and R. Xiao, *Int. J. Hydrogen Energy*, 2016, **41**, 22711–22721.
7 D. Zeng, R. Xiao, S. Zhang and H. Zhang, *Fuel Process. Technol.*, 2015, **139**, 1–7.
8 K. Kang, C. Kim, K. Bae, W. Cho, S. Kim and C. Park, *Int. J. Hydrogen Energy*, 2010, **35**, 12246–12254.
9 K. Svoboda, A. Siewiorek, D. Baxter, J. Rogut and M. Punčochář, *Chem. Pap.*, 2007, **61**, 110–120.
10 S. Takenaka, N. Hanaizumi, V. T. D. Son and K. Otsuka, *J. Catal.*, 2004, **228**, 405–416.
11 P. Chiu and Y. Ku, *Aerosol Air Qual. Res.*, 2012, **12**, 1421–1432.
12 P. Chiesa, G. Lozza, A. Malandrino, M. Romano and V. Piccolo, *Int. J. Hydrogen Energy*, 2008, **33**, 2233–2245.

13 D. Zeng, Y. Qiu, S. Peng, C. Chen, J. Zeng, S. Zhang and R. Xiao, *J. Mater. Chem. A*, 2018, **6**, 11306–11316.

14 Z. Huang, F. He, Y. Feng, K. Zhao, A. Zheng, S. Chang, G. Wei, Z. Zhao and H. Li, *Energy Fuels*, 2013, **28**, 183–191.

15 Q. Chen, S. Hu, J. Xiang, S. Su, L. Sun, Y. Wang, L. Zhang and H. Chi, *Fuel Process. Technol.*, 2016, **146**, 56–61.

16 M. Ismail, W. Liu and S. A. Scott, *Energy Procedia*, 2014, **63**, 87–97.

17 R. V. Siriwardane, E. Ksepko, H. Tian, J. Poston, T. Simonyi and M. Sciazko, *Appl. Energy*, 2013, **107**, 111–123.

18 S. Sun, M. Zhao, L. Cai, S. Zhang, D. Zeng and R. Xiao, *Energy Fuels*, 2015, **29**, 7612–7621.

19 Z. Yu, Y. Yang, S. Yang, Q. Zhang, J. Zhao, Y. Fang, X. Hao and G. Guan, *Carbon Resour.*, 2019, **2**, 23–34.

20 H. Leion, E. Jerndal, B. Steenari, S. Hermansson, M. Israelsson, E. Jansson, M. Johnsson, R. Thunberg, A. Vadenbo, T. Mattisson and A. Lyngfelt, *Fuel*, 2009, **88**, 1945–1954.

21 T. Song, T. Shen, L. Shen, J. Xiao, H. Gu and S. Zhang, *Fuel*, 2013, **104**, 244–252.

22 H. Leion, A. Lyngfelt and T. Mattisson, *Chem. Eng. Res. Des.*, 2009, **87**, 1543–1550.

23 D. Zeng, R. Xiao, Z. Huang, J. Zeng and H. Zhang, *Int. J. Hydrogen Energy*, 2016, **41**, 6676–6684.

24 R. Xiao, S. Zhang, S. Peng, D. Shen and K. Liu, *Int. J. Hydrogen Energy*, 2014, **39**, 19955–19969.

25 Z. Huang, F. He, Y. Feng, R. Liu and K. Zhao, *Int. J. Hydrogen Energy*, 2013, **38**, 14568–14575.

26 Z. Yu, C. Li, Y. Fang, J. Huang and Z. Wang, *Energy Fuels*, 2012, **26**, 2505–2511.

27 Z. Huang, F. He, K. Zhao, A. Zheng, H. Li and Z. Zhao, *Prog. Chem.*, 2012, **24**, 1599–1609.

28 J. Lachén, J. Plou, P. Durán, J. Herguido and J. A. Peña, *Int. J. Hydrogen Energy*, 2017, **42**, 13607–13616.

29 L. Wang, L. Shen, W. Liu and S. Jiang, *Energy Fuels*, 2017, **31**, 8423–8433.

30 W. Liu, L. Shen, H. Gu and L. Wu, *Energy Fuels*, 2015, **30**, 1756–1763.

31 H. Gu, S. Lang, G. Song, S. Zhang, M. Niu, W. Liu and L. Shen, *Chem. Eng. J.*, 2019, **360**, 260–270.

32 J. Bao, Z. Li and N. Cai, *Ind. Eng. Chem. Res.*, 2013, **52**, 6119–6128.

33 H. Gu, L. Shen, J. Xiao, S. Zhang, T. Song and D. Chen, *Combust. Flame*, 2012, **159**, 2480–2490.

34 M. M. Hossain and H. I. de Lasa, *Chem. Eng. Sci.*, 2008, **63**, 4433–4451.

35 T. Mendiara, A. Abad, L. F. de Diego, F. García-Labiano, P. Gayán and J. Adánez, *Chem. Eng. J.*, 2019, **359**, 37–46.

36 M. A. Pans, P. Gayán, L. F. de Diego, F. García-Labiano, A. Abad and J. Adánez, *Chem. Eng. Res. Des.*, 2015, **93**, 736–746.

37 X. Wang, Z. Chen, M. Hu, Y. Tian, X. Jin, S. Ma, T. Xu, Z. Hu, S. Liu, D. Guo and B. Xiao, *Chem. Eng. J.*, 2017, **312**, 252–262.

38 H. Shin, S. Choi, K. Jung and S. Han, *Chem. Mater.*, 2001, **13**, 1238–1242.

39 D. Zeng, R. Xiao, S. Zhang and H. Zhang, *Fuel Process. Technol.*, 2015, **139**, 1–7.

40 Z. Gu, K. Li, S. Qing, X. Zhu, Y. Wei, Y. Li and H. Wang, *RSC Adv.*, 2014, **4**, 47191–47199.

41 B. Wang, R. Yan, H. Zhao, Y. Zheng, Z. Liu and C. Zheng, *Energy Fuels*, 2011, **25**, 3344–3354.

42 X. Niu, L. Shen, S. Jiang, H. Gu and J. Xiao, *Chem. Eng. J.*, 2016, **294**, 185–192.

43 S. Jiang, L. Shen, J. Wu, J. Yan and T. Song, *Chem. Eng. J.*, 2017, **317**, 132–142.

44 A. M. Banerjee, M. R. Pai, S. S. Meena, A. K. Tripathi and S. R. Bharadwaj, *Int. J. Hydrogen Energy*, 2011, **36**, 4768–4780.

45 K. Li, M. Haneda, Z. Gu, H. Wang and M. Ozawa, *RSC Adv.*, 2013, **93**, 129–132.

46 K. Li, H. Wang, Y. Wei and D. Yan, *Chem. Eng. J.*, 2010, **156**, 512–518.

47 X. Zhu, K. Li, Y. Wei, H. Wang and L. Sun, *Energy Fuels*, 2014, **28**, 754–760.